CAMBRIDGE
UNIVERSITY PRESS

Research Article

Milliarcsecond structures of variable-peaked spectrum sources

K. Ross[1] ⬩, C. Reynolds[2] ⬩, N. Seymour[1] ⬩, J. R. Callingham[3,4] ⬩, N. Hurley-Walker[1] ⬩, and H. Bignall[5,2] ⬩

[1]International Centre for Radio Astronomy Research, Curtin University, Bentley, WA 6102, Australia, [2]CSIRO, Space and Astronomy, P.O. Box 1130, Bentley, WA 6102, Australia, [3]Leiden Observatory, Leiden University, PO Box 9513, Leiden, 2300 RA, The Netherlands, [4]ASTRON, Netherlands Institute for Radio Astronomy, Oude Hoogeveensedijk 4, Dwingeloo, 7991 PD, The Netherlands and [5]Manly Astrophysics, 15/41-42 East Esplanade, Manly, NSW 2095, Australia

Abstract

Spectral variability offers a new technique to identify small scale structures from scintillation, as well as determining the absorption mechanism for peaked-spectrum (PS) radio sources. In this paper, we present very long baseline interferometry (VLBI) imaging using the long baseline array (LBA) of two PS sources, MRC 0225–065 and PMN J0322–4820, identified as spectrally variable from observations with the Murchison Widefield Array (MWA). We compare expected milliarcsecond structures based on the detected spectral variability with direct LBA imaging. We find MRC 0225–065 is resolved into three components, a bright core and two fainter lobes, roughly 430 pc projected separation. A comprehensive analysis of the magnetic field, host galaxy properties, and spectral analysis implies that MRC 0225–065 is a young radio source with recent jet activity over the last 10^2–10^3 yr. We find PMN J0322–4820 is unresolved on milliarcsecond scales. We conclude PMN J0322–4820 is a blazar with flaring activity detected in 2014 with the MWA. We use spectral variability to predict morphology and find these predictions consistent with the structures revealed by our LBA images.

Keywords: quasars: general – quasars: individual – galaxies: active – radio continuum: galaxies – galaxies: structure – galaxies: jets

1. Introduction

Peaked-spectrum (PS) sources are a subset of active galactic nuclei (AGN) that are identified by a peak in their radio spectral energy distribution (O'Dea & Saikia 2021) and are also often associated with compact morphologies ($\lesssim$20 kpc; Phillips & Mutel 1982; Tzioumis et al. 2010). PS sources provide an interesting population of AGN as the evolutionary pathway from PS source to extended ($\gtrsim$30 kpc) AGN is still unclear. Two contending theories hypothesise the nature and evolutionary pathway of PS sources: the *youth scenario*, where the age of the PS source is $\leq 10^5$ yr and has not yet had ample time to grow to the large-scale AGN (O'Dea & Baum 1997; Owsianik & Conway 1998; Tinti & de Zotti 2006); and the *frustration scenario*, when the PS source is confined by a dense cloud of the interstellar medium (ISM) of the host galaxy environment (van Breugel, Miley, & Heckman 1984; Wilkinson et al. 1984; O'Dea, Baum, & Stanghellini 1991). Furthermore, recent identifications of embedded PS cores within remnant ageing lobes has been attributed to restarted and episodic AGN activity (Hernández-García et al. 2019), i.e. a cyclical evolution rather than linear evolution.

Compact symmetric objects (CSOs) are a subset of PS sources with similar morphologies to large scale AGN, namely a central region (often quite faint, if detected) with emission either side associated with hot spots and/or lobes. Unlike typical AGN, CSOs show emission only on very compact scales, typically $\leq$1 kpc, and thus require high-resolution imaging to detect (Phillips & Mutel

1982; Gugliucci et al. 2005). CSOs are generally considered young AGN ($<10^4$ yr; O'Dea & Baum 1997; Owsianik & Conway 1998; Tinti & de Zotti 2006), which may evolve into typical, radio-loud AGN.

Previous attempts to discriminate between youth and frustration scenarios have relied on spectral modelling and high-resolution imaging (e.g. Marr et al. 2014; Keim, Callingham, & Röttgering 2019) using very long baseline interferometry (VLBI). The cause of absorption at low frequencies, producing the spectral peak, has typically been attributed to synchrotron-self absorption (SSA) and/or free-free absorption (FFA) for the youth and frustration scenarios respectively (Tingay & de Kool 2003; Callingham et al. 2015). Unfortunately, without sufficient sampling below the spectral turnover, the cause of absorption is often ambiguous (Callingham et al. 2017). In rare cases, a SSA model can be ruled out if the optically thin spectral index is sufficiently steep ($\alpha \geq 2.5$).[a]

Many PS sources have been identified as a CSOs (e.g. 0108+388, 0710+439 and 2352+495; Readhead et al. 1996). As CSOs are typically considered to be young AGN, identifying PS sources that are also CSOs could help to differentiate between the youth and frustrations scenarios. However, identifying CSOs requires high resolution (mas) observations using VLBI. Likewise, PS sources sometimes display extremely asymmetrical mas structures, likely due to an inhomogeneous surrounding environment influencing their growth (Orienti et al. 2006; Keim et al. 2019), compared with a fairly symmetrical morphology associated with CSOs with minor asymmetries likely coming from orientation effects (Orienti & Dallacasa 2008). VLBI can

[a]We assume a power-law relation where $S_\nu = S_0 \nu^\alpha$, thus the sign of α, being negative or positive, also indicates either the optically thin or thick spectral index respectively.

also be used to measure proper motion of hot-spots in lobes to estimate kinematic ages of $\leq 3 \times 10^3$ yr (Polatidis & Conway 2003; Gugliucci et al. 2005), consistent with the theory that CSOs are young AGN. Indeed, Gugliucci et al. (2005) find a majority of the CSOs with age estimates were ≤ 500 yr, suggesting CSOs may be short lived and few would continue to grow to the scale of typical AGN, thereby explaining the large fraction of CSO and PS sources thought to be young relative to the number of large-scale radio galaxies (O'Dea & Saikia 2021). VLBI of PS sources can thus help to identify populations of CSOs and elucidate the youth scenario and AGN evolution.

Spectral variability at radio frequencies offers a new technique for identifying young or frustrated candidates. Many variability surveys have identified PS sources that lost their PS classification over time (Tinti et al. 2005; Torniainen et al. 2005; Ross et al. 2021, hereafter R21), or showed a significant change in spectral shape likely due to a variable opacity from the inhomogeneous surrounding ISM (Tingay et al. 2015; Ross et al. 2022, hereafter R22). Thus the population of known PS sources, which is already biased from sparse spectral coverage from a range of instruments and times, is likely contaminated by temporary PS sources. This is particularly true at higher frequencies ($\sim$GHz), which is sensitive to emission from the core/jets. PS sources with a peak at lower frequencies ($\sim$MHz) appear to be less contaminated by sources only showing a temporary peak (Callingham et al. 2017, R21).

Spectral variability offers the a new technique to find and exclude contaminating 'temporary' PS sources, as well as identify CSO candidates with a decreased risk of contaminating sources. Variability of PS sources has been used to infer the presence of compact (μas – mas) features based on scintillation (Fanti et al. 1979; Chhetri et al. 2018, R21). Such compact features are common for CSOs, but VLBI is required for confirmation of a CSO classification. Spectral variability has also found PS sources that show changing spectral shape, inconsistent with scintillation, which suggests that some PS sources are frustrated or contaminating blazars (R22).

This paper aims to investigate the milliarcsecond scale structures of variable PS sources using VLBI to test predictions based on spectral variability. In particular, we investigate PS sources that have shown a consistent spectral shape with a variable overall flux density, consistent with scintillation, suggesting a compact feature on milliarcsecond scales (R21, R22), and use VLBI to test a CSO classification. We also investigate variable PS sources that R21 found as changing spectral shape. They concluded the short timescale ($\sim$1 yr), and variable spectral shape is inconsistent with interstellar scintillation and present it as a blazar caught flaring.

In Section 2, we describe the three variable PS sources of this study. In Section 3, we describe the observational strategy and data reduction. Section 4 outlines the results of the LBA imaging. We discuss the host galaxy properties including their linear size compared to turnover in Section 5.1, the mid-infrared (MIR) and optical emission in Section 5.2 and the radio properties in Section 5.3. In Section 6, we present the likely absorption mechanisms and source classification of our targets. We adopt the standard Λ-cold dark matter cosmological model, with $\Omega_M = 0.286$, $\Omega_\Lambda = 0.714$, and the Hubble constant $H_0 = 69.6$ km s^{-1} Mpc^{-1} (Wright 2006; Hinshaw et al. 2013)

2. Target selection

Targets were selected for LBA imaging with the goal of comparing direct imaging of milliarcsecond structures with predicted

Table 1. LBA stations included in observations.

Name	Code	Diameter (m)	Nov20	Feb21
ATCA, phased up	At	5×22	Y	Y
Mopra	Mp	22	Y	Y
Parkes	Pa	64	Y	Y
Hobart	Ho	26	Y	Y
Ceduna	Cd	30	Y	Y
Yarragadee	Yg	12	Y	Y
Warkworth	Ww	12	Y	Y
Hartebeesthoek	Hh	26	Y	Y
Katherine	Ke	12	Y	Y
Tidbinbilla	Td	34	Y	N

morphologies based on their variability. Three targets were selected based on the variability detected by R21 and R22. MRC 0225–065 (GLEAM J022744-062106) was initially identified as variable in R21 but further monitoring over a year found no evidence of variability (R22). As such, it was predicted MRC 0225–065 would have resolved structures on milliarcsecond scales with a compact feature $\lesssim$25 mas, resulting in variability from refractive interstellar scintillation (RISS) on a longer timescale with a dampened modulation index due to the extended structure. Conversely, PMN J0322–4820 (GLEAM J032237–482010) was selected due to the variable spectral shape identified in R21. To explain the variable spectral shape, R21 concluded PMN J0322–4820 was likely a blazar caught flaring in 2014. As such, it was predicted to show a compact morphology even on milliarcsecond scales. Finally, MRC 2236-454 (GLEAM J223933–451414) was identified by R21 as the only PS source in their sample that showed significant variability but maintained a constant peak frequency below 231 MHz. A low peak frequency is typically associated with PS sources that are of the order of tens of kilo-parsecs across, but the RISS detected by R22 suggested MRC 2236-454 is dominated by a compact feature, and showed variability due to a surrounding inhomogeneous environment. As such, it was predicted MRC 2236-454 may be resolved on milliarcsecond scales and show an asymmetrical morphology, often associated with frustrated sources in an inhomogeneous surrounding environment (Orienti et al. 2006).

3. LBA observations and data reduction

3.1 Observations

LBA observations were taken on 2020 November 23 and 2021 February 17 as part of project V600. The November observation was centered at 2.4 GHz and the February observation was centered at 8.3 GHz and both utilised 128 MHz of bandwidth in dual polarizations. Stations used in each observation and their diameter is listed in Table 1. Both observations cycled through phase calibrator scans and target scans of lengths 2 and 5 min, respectively. However, the spatial separation of each target and their respective phase calibrator meant each target had a different number of scans. A summary of the targets, phase calibrators and number of scans each is presented in Table 2.

Parkes at 2.4 GHz, and Katherine at both frequencies, observed using their native linear feeds. These were converted to a circular polarization basis post-correlation using the PolConvert software (Martí-Vidal et al. 2016)

Table 2. Targets, associated calibrators and number of LBA scans for each target source.

Source name	Expected S_{5GHz} (mJy)	Number of scans
MRC 0225–065	0.238	27
PKS J0217+0144 (C)	0.666	27
PMN J0322–4820	0.112	40
PMN J0335-4837 (C)	0.112	40
MRC 2236–454	0.420	48
QSO B2227–445 (C)	0.386	48

3.2 Data processing and calibration

After correlation, data calibration and processing were done using the NRAO's Astronomical Imaging Processing System (AIPS) (Wells 1985). The calibration and flagging followed the general procedure outlined in the AIPS cookbook[b] and was implemented in a semi-automated script with the ParselTongue interface (Kettenis et al. 2006). Initial flagging of edge channels and RFI was done using UVFLG. Auto-correlations were scaled to unity across the band using ACCOR before removing gross residual instrumental delays using FRING on a short scan of a bright calibrator. Complex bandpass corrections were derived using BPASS. The system temperature and gain calibration were applied using APCAL. Delay, rate and phase calibrations were determined from fringe fitting using FRING from each target's respective phase calibrator. A phase referenced image was created for all targets except for MRC 0225–065, as a first pass detection of the targets to determine if a phase shift was needed. Lastly, UVFIX was used to apply a phase shift to the data for any sources that were ~arcsecond away from the phase centre used in correlation. MRC 0225–065 had accurate VLBI coordinates and thus did not require a phase shift. The calibrated and phase shifted data were exported to be imaged using casa.

3.3 Imaging and self-calibration

Initial Stokes-I images were made with a quasi-natural weighting with robust parameter set to +1 (Briggs 1995) using the tclean function in casa (McMullin et al. 2007). Clean boxes were used but were tightly restricted for the models used for self-calibration to avoid inducing artificial structure from the complex point-spread-function. For each image, phase only self calibration was performed and applied using the gaincal and applycal functions, respectively. Due to the sparse (u,v)-coverage and low signal-to-noise (SNR), calibration solutions were inspected and applied without flagging solutions that had insufficient SNR. The slow rate of improvement necessitated several (~9) rounds of self-calibration. The SNR of the main component and the root-mean-squared (rms) noise of the image were inspected after each self calibration iteration to ensure each round improved the overall image quality. For each source the initial model assumed for the self-calibration was an unresolved point source to avoid inducing any morphological features. Any resolved components were included in subsequent rounds of imaging clean components and kept in the model for self-calibration if this reduced the rms noise of the image. The initial solution interval for the self calibration was set

to the scan length and decreased in further rounds of self calibration. Phase only self calibration rounds were continued until the rms noise of the image increased. A final round of both phase and amplitude self calibration was then performed (provided it reduced the rms of the final image) with the solution interval set to the scan length. For MRC 0225–065, an amplitude self-calibration was applied to both frequencies, but no amplitude self-calibration was applied to the 2.4 GHz image of PMN J0322–4820.

4. Results

Images of MRC 0225–065 at both 2.4 and 8.3 GHz are presented in Figure 1, and an image of PMN J0322–4820 at 2.4 GHz, presented in Figure 3. Unfortunately, due to large phase errors from a pointing offset, we were unable to recover images for MRC 2236–454 at either frequency, or for PMN J0322–4820 at 8.3 GHz, this was because the source positions were beyond the observed correlated field of view for recovery in each case. For MRC 2236–454, the pointing offset was over 11 arcsec for both the 2.4 and 8.3 GHz observations, thus the phase errors from this pointing offset was beyond recovery. PMN J0322–4820 also had a pointing offset of ≈11.5 arcsec, however, given it was bright (~0.2 Jy), there was sufficient sensitivity using a subset of antennas (flagging the Hartebeesthoek antenna), and a phase shift combined with self calibration to recover and image at 2.4 GHz. However, this method was not possible at 8.3 GHz due to the smaller field-of-view and decreased sensitivity. Henceforth, we will only discuss the results for MRC 0225–065 and PMN J0322–4820.

4.1 MRC B0225–065

MRC 0225–065 was resolved into three components morphology at both 2.4 and 8.3 GHz, as shown in Figure 1. The final image was made with a robust parameter of -1 at 2.4 GHz and -0.5 at 8.3 GHz (Briggs 1995). MRC 0225–065 is resolved into 3 regions: a bright, unresolved central component, with an upper limit of source size of 2.5×4 mas assuming the beam size at 8.3 GHz (labelled C in Figure 1), a fainter 16×11 mas Western region (L1) and even fainter 14×10 mas Eastern component (L2). The sizes of L1 and L2 are measured using the contours in the 2.4 GHz image. The triple morphology is roughly symmetrical with the distance between the C to L1 and L2 being ~40 mas each. Since it appears the components of MRC 0225–065 may be resolved, we measured their flux density over an irregular polygon[c] for each component.

We recovered all the flux density predictions from the spectral fit to the R22 ATCA observations at 2.4 GHz, but found that ~35% of the flux density was lost at 8.3 GHz. The flux densities for each component and their spectral index are presented in Table 4. The irregular polygon was shaped based on contour levels to ensure only real flux was included in the final measurement. However, the missing flux density at 8.3 GHz may be due to extended structure being resolved out. Consequently, the estimates for the spectral index presented in Table 4 should be considered lower limits.

The symmetrical triple morphology suggests MRC 0225–065 is a CSO candidate with a core (C) and two lobes (L1 and L2). The spectral index of the central component is $\alpha_C = -0.95 \pm 0.08$, which is far steeper than expected for a typical AGN 'core', generally expected to have a $\alpha \geq -0.5$ (Orienti et al. 2006; Hardcastle & Looney 2008). However, components have previously been

---

[b]The AIPS cookbook can be found here http://www.aips.nrao.edu/cook.html.

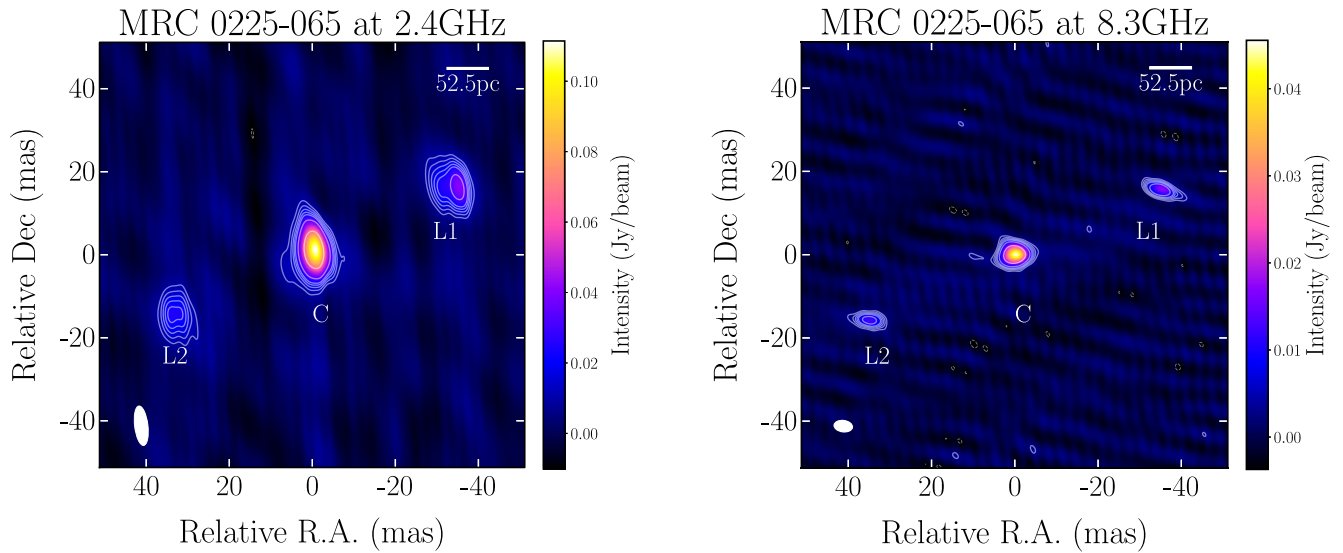[c]using https://github.com/nhurleywalker/polygon-flux (Hurley-Walker et al. 2019).

Figure 1. LBA images of MRC 0225–065 at 2.4 GHz (left) and 8.3 GHz (right). Beam sizes are shown with a white ellipse in the bottom left corner of each image and dimensions are specified in Table 3. Contours are placed at (–3, 3, 4, 5, 6, 7, 10, 20, 50, 100, 200, 400, 800, 1 600) times the rms noise of the image, also specified in Table 3. Pixel brightness is plotted in a linear scale following the colour bars to the right of each image. The resolved regions are labelled C, L1, L2 and properties of each region are outlined in Table 4. Relative R.A and Dec are calculated from the position of the core (C) component with coordinates: J2000 02h27m44.5s -06d21m06.7s.
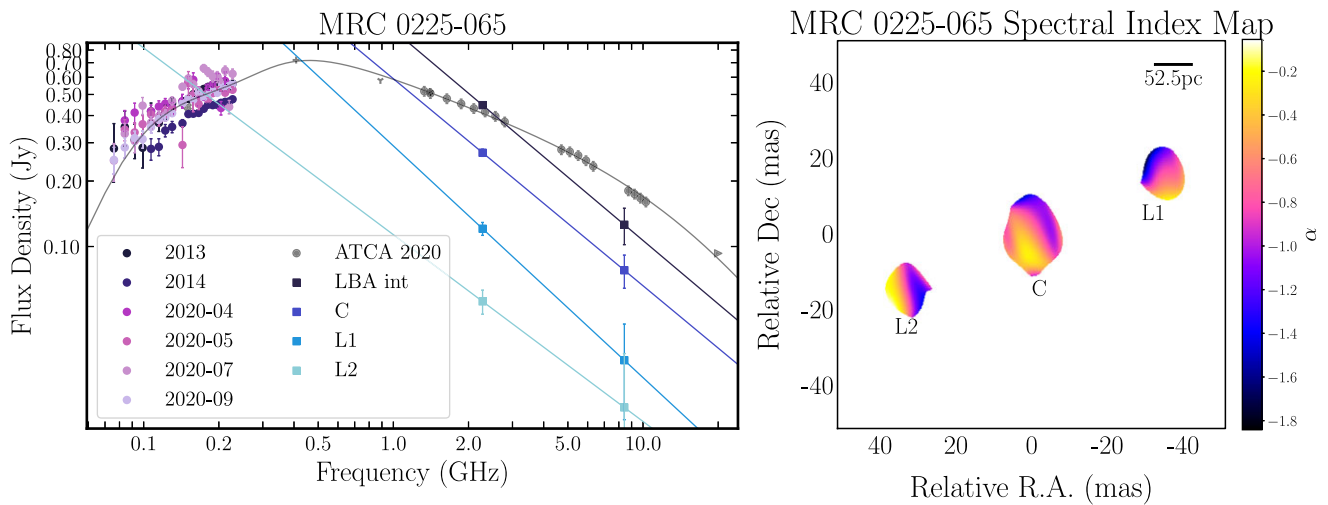

Figure 2. Spectral energy distribution (SED) for MRC 0225–065 (left) and spectral index map (right). The spectral index map was created using by convolving both the 8.3 GHz image and 2.4 GHz image to the same resolution. Data included in the SED are from R21 and R22 monitoring (circles) and coloured according to epoch. LBA flux densities are plotted as squares with the integrated flux density of LBA plotted as black squares. The spectral fit to each LBA point is a power-law with spectral index presented in Table 4. The grey spectral model to the entire SED is a double SSA model with an exponential break. Supplementary data included: TIFR GMRT 150 MHz Sky Survey Alternative Data Release 1 (TGSS-ADR1; Intema et al. 2017) (grey cross), Molonglo Reference Catalogue (MRC; Large et al. 1981; Large, Cram, & Burgess 1991) (grey +), Rapid ASKAP Continuum Survey (RACS; McConnell et al. 2020; Hale et al. 2021) (grey 'Y'), NRAO VLA Sky Survey NVSS; (NVSS; Condon et al. 1998), Australia Telescope 20 GHz (AT20G; Murphy et al. 2010) (grey right arrow).

identified as cores with spectral indices as steep as −0.7 (Orienti et al. 2006). We present the SED for MRC 0225–065 in Figure 2 including the MWA flux densities from R22 as well as the flux densities and power-law spectral model for each LBA component. The entire SED is fit, using the most recent MWA epoch (2020-09), with a double SSA model with an exponential break, which assumes two synchrotron emitting regions that are self-absorbed and ageing producing the exponential break, ν_b, separate from the peak frequency. The break frequency is the frequency where the spectrum begins to steepen as the electrons are ageing and experiencing energy losses (Turner, Shabala, & Krause 2018). We

fit the spectral model using the UltraNest package[d] (Buchner 2021), which uses a nested sampling Monte Carlo algorithm. From the double SSA spectral model, we find the peak frequencies for the two SSA components to be $\nu_{p,1} = 400 \pm 100$ MHz and $\nu_{p,2} = 112 \pm 90$ MHz, and find $\nu_b = 14.3 \pm 2.7$ GHz.

MRC 0225–065 has a spectroscopic redshift of 0.445 (Albareti et al. 2017); thus, 1 mas corresponds to a linear scale of 5.25 pc. Using this redshift, we find the projected linear size of MRC 0225–065 (from L1 to L2) to be ∼430 pc, the linear distance from the
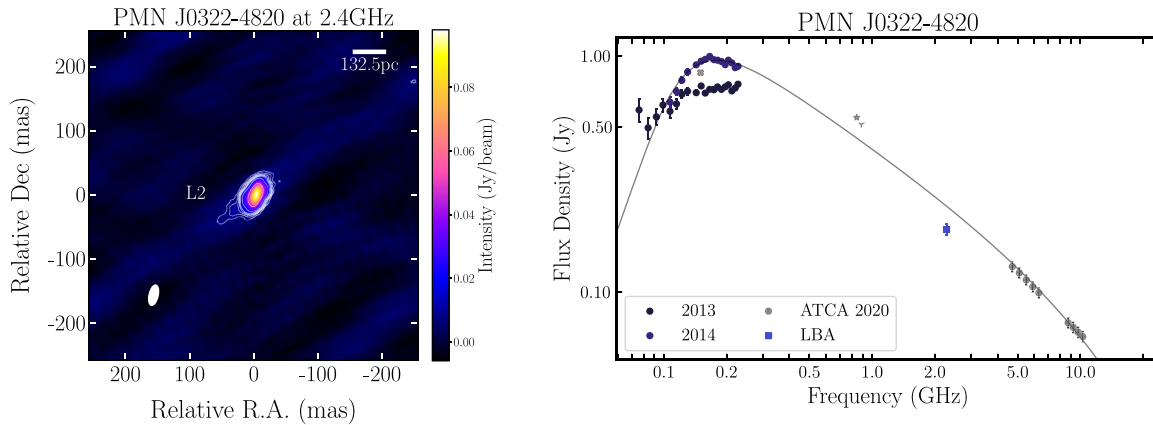
Figure 3. LBA image for PMN J0322–4820 at 2.4 GHz (left) and associated SED (right). The beam size is shown with a white ellipse in the bottom left corner and dimensions are specified in Table 3. Contours are placed at (–3, 3, 4, 5, 6, 7, 10, 20, 50, 100, 200, 400, 800, 1 600) times the rms noise of the image, also specified in Table 3. Pixel brightness is plotted in a linear scale following the colour-bars to the right of the image. Relative R.A and Dec are calculated from the central coordinate: J2000 03h22m38.0s -48d20m16.2s. Data included in SED is from R21 and R22 (circles) and coloured according to epoch. LBA flux density is plotted as a blue square. The grey spectral model to the entire SED is a single SSA model with an exponential break. Supplementary data included is: TIFR GMRT 150 MHz Sky Survey Alternative Data Release 1 (TGSS-ADR1; Intema et al. 2017) (grey cross), Sydney University Molonglo Sky Survey (SUMSS; Mauch et al. 2003) (grey star), Rapid ASKAP Continuum Survey (RACS; McConnell et al. 2020; Hale et al. 2021) (grey 'Y').

Table 3. Properties for each LBA image: synthesised beam size and rms background noise.

Source, ν (GHz)	rms (mJy beam^{-1})	$\theta_{beam,maj}$	$\theta_{beam,min}$	PA
MRC 0225–065, 2.4	2.7	9.5	3.2	7.0
MRC 0225–065, 8.3	1.0	4.4	2.7	83
PMN J0322–4820, 2.4	1.0	30	17	–54

core to either lobe to be ∼210 pc and place an upper limit on the size of component C to be ≤26 pc.

4.2 PMN J0322–4820

Due to difficulties in the phase calibration, we were only able to produce a high quality image of J0322–483 at 2.4 GHz, shown in Figure 3. We do not resolve PMN J0322–4820 and it is confined to the size of the beam: 56 × 40 mas. The final image was made using a robust parameter of +0.5, and by flagging the Hartebeesthoek antenna, thus the beam size for PMN 0322–4820 compared to MRC 0225–065 for the same frequency is much larger. Details of the image properties are presented in Table 3. Compared to the spectral model fit to the ATCA and 2014 MWA observations, 18% of the flux density was missing. We used a reported photometric redshift for PMN J0322–4820 of 0.16 (Bilicki et al. 2014), thus 1 mas corresponds to a linear size of 2.650 pc. We place an upper limit on the source size of 148 pc.

5. Discussion

In this section, we will present a comprehensive analysis of both MRC 0225–065 and PMN J0322–4820 to produce a unified perspective of these two sources with the aim of concluding whether they are young or frustrated PS sources. In Section 5.1, we present our two sources in the linear size and turnover relation, in Section 5.2, we discuss the host galaxy properties according to mid-infrared, optical observations and radio properties.

Table 4. Flux densities and two component spectral index for each component of MRC 0225–065 found in the LBA images. The uncertainties for the flux densities are measured calculated using the measured uncertainty from polygon flux and the rms noise of the image. The uncertainty for α is calculated using standard propagation of errors. The model prediction is calculated from the best spectral fit, a double SSA spectral model with an exponential break.

Component	$S_{2.4GHz}$ (mJy)	$S_{8.3GHz}$ (mJy)	α
C	270±10	78±7	−0.95±0.08
L1	121±8	30±5	−1.1±0.2
L2	56±7	18±4	−0.9±0.2
Integrated LBA	447±14	126±10	−0.97±0.07
Model prediction	400	195	N/A

5.1 Linear size and turnover relation

PS sources follow an inverse relation between their linear size and intrinsic turnover frequency, often referred to as the linear size turnover relation, first presented by O'Dea (1998). This relation is directly predicted from the youth scenario (O'Dea 1998) where the peak frequency is due to SSA and thus the linear size is directly related to the peak frequency (Kellermann & Pauliny-Toth 1981). While modifications to models in the frustration scenario can reproduce this relation (Bicknell et al. 2018), it is generally understood that PS sources that fall below the linear size-turnover relation are likely compact beyond what is expected for a young source and a thus assumed to be frustrated. We plot both MRC 0225–065 and PMN J0322–4820 on the linear size-turnover relation in Figure 4, along with other known PS sources, details of which are discussed by Keim et al. (2019). It is evident from Figure 4, that MRC 0225–065 is entirely consistent with the relation whereas PMN J0322–4820 sits somewhat below the relation, particularly since the linear size is an upper limit. This would suggest MRC 0225–065 is consistent with the youth scenario whereas PMN J0322–4820 may be frustrated. However, it is worth nothing, R21 identified PMN J0322–4820 as a variable PS source with a changing spectral shape, and thus concluded it was likely a blazar. Furthermore, R21 found the peak frequency changed from ∼320
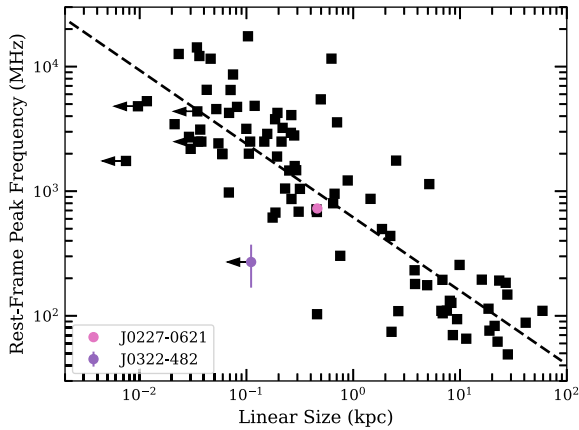
Figure 4. Rest frame peak frequency versus linear size. Sources in black are described in Keim et al. (2019). The dashed line is the fit to the relation found by Orienti & Dallacasa (2014). Arrows indicate maximum linear sizes for unresolved sources. MRC 0225–065 (pink circle) and PMN J0322–4820 (purple circle) are plotted with linear sizes calculated from LBA images. The error bars for MRC 0225–065 represent the range for peak frequencies calculated in R21.

MHz in 2013 to ~145 MHz in 2014. As the peak frequency is variable and PMN J0322–4820 is known to exhibit a changing spectral shape, its position on the linear size-turnover relation will also vary, shown by the error bar in Figure 4 corresponding to the range of the peak frequency from 2013 to 2014. Most likely, PMN J0322–4820 is only a temporary PS source and thus should not be included in this relation nor when considering the PS population at large.

5.2 Host galaxy properties

5.2.1 WISE colours

MIR colour selection techniques using the *Wide-Field Infrared Survey Explorer* (Wright et al. 2010, WISE) are widely used to efficiently distinguish between AGN and star-forming galaxies.

WISE is a MIR all sky survey covering four photometric bands: 3.4, 4.6, 12, and 22 μm referred to as W1, W2, W3, and W4, respectively. The MIR wavelengths are sensitive to the emission from hot dust in the torus of the AGN, allowing for the identification of AGN where X-ray and optical emission may be blocked by intervening gas and dust. This also makes AGN stand out from star-bursting galaxies or stars due to their extremely red MIR emission (Lonsdale et al. 2015). Obscured AGN with red MIR emission have been identified by their MIR colours, often by their place in a colour-colour diagram (Jarrett et al. 2011; Lonsdale et al. 2015). The bulk of sources centred around $W1 - W2 = 1.2$ and $W2 - W3 = 3$ correspond to the region typically associated with quasars and AGN. MRC 0225–065 is found in the region typically associated with emission from star formation or stellar emission; i.e. there is no evidence of hot AGN dust, however, there is evidence for moderate star formation. As we know MRC 0225–065 is an AGN, it is likely the emission at MIR is a combination of these two processes.

PMN J0322–4820 is well within the elliptical regime, thus has low emission from star formation and no evidence of hot AGN dust. Blazars are typically found to dominate the top right region of the *WISE* colour-colour plot as the MIR emission is dominated by the emission of the blazar over the galaxy (and associated stellar emission). A compact morphology and variable spectral shape

suggest PMN J0322–4820 is a blazar. However, the *WISE* colours of PMN J0322–4820 suggest that the host galaxy is an elliptical with predominantly red optical emission. Therefore, the emission from the potential radio blazar is not dominant in the MIR. While it is more common to find blazars in the top right region of the *WISE* colour-colour plot, the MIR colours, which suggest the host galaxy for PMN J0322–4820 is an elliptical, are still consistent with a blazar classification (Yang, Chen, & Huang 2015; D'Abrusco et al. 2019).

5.2.2. Optical spectra

MRC 0225–065 has an optical spectrum from the 13th data release of the Sloan Digital Sky Survey (Albareti et al. 2017, SDSS). From the fitted spectrum, Albareti et al. (2017) report a spectroscopic redshift for MRC 0225–065 of $z = 0.445$ and classify it as a broad-line, starburst quasar. The spectrum additionally has low-ionisation nuclear emission-line region (LINER) properties, evident from the strong NII, SiII, and OI lines. A LINER has a high energy radiation field. There is still debate about whether this is AGN emission or star formation, but likely the combination of the broad lines, strong OIII emission and radio-loudness of MRC 0225–065 is evidence of AGN. From the broad Hα, we can calculate the velocity dispersion according to:

$$d(\text{velocity}) = c \frac{d(\lambda)}{\lambda_0}, \tag{1}$$

where c is the speed of light, $d(\lambda)$ is the wavelength dispersion from the spectral fit, and λ_0 is the rest-frame wavelength of Hα. Using the reported fit to the broad Hα from SDSS where $\lambda_{\text{observed}} = 9\,486$ Å, we use the equivalent width, EW$= 30 \pm 4$ Å, and find the velocity dispersion to be 900 ± 100 km s^{-1}. This large velocity dispersion may be from an extreme star formation wind but it is also indicative of the broad-line regions from an AGN, which is more consistent given our radio observations identify MRC 0225–065 as an AGN. The broad Hα, and large velocity dispersion, is consistent with an AGN that is quite obscured, as reported by Albareti et al. (2017) who classify it as a broad-line quasar. Perhaps of more interest are the starburst properties of MRC 0225–065, namely OII and OIII emission lines, identified by Albareti et al. (2017). Both OII and OIII are forbidden lines with different origins: OII is mostly due to star formation and thus is often used as an indicator for star formation in galaxies; OIII is due to an AGN and can be used as a proxy for the AGN bolometric luminosity. This is also consistent with the *WISE* colours discussed in Section 5.2.1, which find MRC 0225–065 consistent with a galaxy with emission coming from both the AGN and star formation. Combining the radio, MIR and optical properties of MRC 0225–065, it is likely this galaxy has moderate star formation with an obscured AGN.

5.3 Radio properties of MRC B0225–065

Combining the spectral information and high resolution resolved structure of MRC 0225–065, we are able to determine several intrinsic properties that can help differentiate between SSA and FFA models. In this section, we estimate the magnetic field strength and spectral ages to assess whether MRC 0225–065 is consistent with the youth scenario. We do not consider PMN J0322–4820 in this section due to its unresolved morphology (even on mas scales) and since the radio variability suggests it is a blazar with an added beaming effect producing Doppler boosting and

thus many of the assumptions required for these calculations no longer hold.

5.3.1 Magnetic field

As a means of evaluating the validity of SSA compared to an FFA, we can calculate the magnetic field estimates based on a pure SSA model and on equipartition. Equipartition assumes there is equal energy between the radiating particles and the magnetic field. The comparison between magnetic field estimates based on an SSA model and equipartition has been used as evidence both for the SSA model (when the estimates are in agreement; Orienti & Dallacasa 2008) and against (when there is a clear disparity; Keim et al. 2019). In this section, we will first estimate the magnetic field assuming a purely SSA model, then assuming equipartition and compare these to determine whether SSA is a reasonable model for MRC 0225−065.

We can estimate the magnetic field strength, in Gauss, based on a purely SSA spectral model, B_{SSA}, according to:

$$B_{SSA} \approx \frac{(\nu_{peak}/f(\alpha_{thin}))^5 \theta_{src,min}^2 \theta_{src,max}^2}{S_{peak}^2(1+z)}, \quad (2)$$

where ν_{peak} is the observed peak frequency in GHz, S_{peak} is the flux density in Jy at the peak frequency for the source at redshift z with angular minor and major component axis, $\theta_{src,min}$ and $\theta_{src,max}$, in mas (Kellermann&Pauliny-Toth 1981). We note, $f(\alpha_{thin})$ is as defined by Kellermann & Pauliny-Toth (1981), where it is loosely related to α_{thin}. We take $f(\alpha_{thin}) = 8$ based on values from Marscher (1983), Orienti & Dallacasa (2008).

Now, assuming equipartition, we calculate the magnetic field strength, in Gauss, according to Miley (1980), as B_{equi} by assuming the component has cylindrical symmetry such that the width of the source on the sky is equivalent to the line of sight path-length.

For both calculations, we calculate B_{SSA} and B_{equi} for the compact core region rather than the total source, to ensure we are comparing a homogeneous region (Orienti & Dallacasa 2008; Keim et al. 2019). For MRC 0225−065, using Equation (2), we estimate the magnetic field strength for a purely SSA model to be $B_{SSA} \approx 6\pm7$ mG for the core region where $\theta_{src} = 2.5 \times 4$ mas. To estimate B_{equi}, we assume a filling factor $\eta = 1$ and set $k = 1^e$ and find $B_{equi} \approx 6\pm2$ mG. As B_{SSA} is within the uncertainties of B_{equi}, it suggests the core region of MRC 0225−065 is in equipartition and consistent with a pure SSA model. While this does not exclude the FFA model, it does provide supportive evidence for the SSA model. Furthermore, it may not be a valid assumption that MRC 0225−065 is in equipartition, thus the equation from Miley (1980) for B_{equi} would not be a reasonable estimate of the magnetic field strength.

We can also use the estimated magnetic field to calculate the age of the electron population as a proxy for the age of the jets/lobes. Calculating the spectral age of the electron population requires an accurate estimate of the break frequency, ν_b. We can thus calculate the spectral age, τ_{spec}, according to:

$$\tau_{spec} = \frac{aB^{1/2}}{B^2 + B_{iC}^2} \left[\nu_b(1+z)\right]^{-1/2}$$

$^e k = 1$ is equivalent to the minimum energy condition, however values for k have ranged from 1 to 100, where $k = 100$ produces an order of magnitude difference in B_{equi} (Pacholczyk & Roberts 1971; Miley 1980).

where

$$B_{iC} = 0.318(1+z)^2$$

$$a = \left(\frac{243\pi m_e^5 c^2}{4\mu_0^2 e^7}\right)^{1/2} \quad (3)$$

where B_{iC} is the magnitude of the microwave background magnetic field in nT, B is the magnetic field of the source in nT, ν_b is the break frequency in GHz, and the constants m_e, c, μ_0, and e are the mass of an electron, speed of light, magnetic permeability of free space, and charge of an electron, respectively.

It is possible the core is actually an unresolved double of more recent AGN activity than the outer lobes, producing the steep ($\alpha \lesssim -1$, see Table 4) spectral index. We assume a constant expansion speed, v, and use the linear sizes to estimate the dynamical age, τ_{dyn}, of the core and outer lobes. Using the magnetic field calculated for the core region assuming equipartition, i.e. setting $B = B_{equi} = 6 \pm 2$ mG, and determining a break frequency, we can estimate the spectral age of the core. Using a break frequency of $\nu_b = 14.3 \pm 2.7$ GHz, calculated from the double SSA spectral model fit, we estimate the spectral age of the core to be $\tau_{spec} \approx 700 \pm 100$ yr. We then calculate an upper limit on the expected expansion velocity of $v \leq 0.13\,c$ (using simple speed = distance/time arguments) for the core using the upper limit for the linear source size of $\theta_{src} \leq 26$ pc, as outlined in Section 4.1. An expansion velocity of $v = 0.13\,c$ is well within previous measurements of the expansion speeds for compact AGN that have been found to range from $0.1\,c$ up to $0.7\,c$ (Polatidis & Conway 2003; An & Baan 2012; Orienti & Dallacasa 2020). The range of expansion velocities would correspond to a range in dynamical ages for the core of $100 \lesssim \tau_{dyn} \lesssim 900$ yr. If we assume the expansion velocity of the core of 'inner lobes' is roughly equal to that of the outer lobes from a previous epoch of activity, we can place an upper limit on the dynamical ages of the outer lobes. We calculate the distance between the core and L1 as ∼210 pc, which corresponds to a dynamical age of 5 000 yr for an expansion velocity of 0.13 c. For the range of dynamical ages for typical PS sources, we expect the age of the outer lobes to be $1\,000 \lesssim \tau_{dyn} \lesssim 7\,000$ yr. Previous estimates for the ages of PS sources using similar assumptions have estimated ages from ∼10^1 to ∼10^5 yr (Orienti, Murgia, & Dallacasa 2010), which is entirely consistent with our age estimates for both the inner core and outer lobes.

As the ages, expansion velocities, and magnetic fields that we calculate are all consistent with the SSA model and a youth scenario, it appears MRC 0225−065 is more consistent with a young CSO rather than a frustrated compact AGN. However, there are several caveats and assumptions made in these calculations. Thus, while these results are consistent with the evolutionary scenario of MRC 0225−065 being the youth model, it is not sufficient for excluding the frustration scenario entirely.

6. A unified perspective of MRC B0225−065 and PMN J0322−4820

Combining all the information we have obtained about MRC 0225−065, we begin to create a unified perspective that suggests MRC 0225−065 is a CSO with a peaked spectrum best explained by SSA and recent jet activity over the last 10^2–10^3 yr. A summary of the evidence in support of this conclusion are as follows:

Variability: R21 identified spectral variability of MRC 0225−065 with a constant spectral shape, consistent with variability due to

RISS. Further spectral variability monitoring by R22 detected no further variability, suggesting a resolved structure but consistent PS source classification. This observation suggests it is unlikely MRC 0225–065 is a contaminating blazar or source with only a temporary PS source classification, such as frustrated sources with an inhomogeneous surrounding medium.

Radio morphology: Previously, it has been suggested frustrated PS sources are more likely to show an asymmetrical morphology due to the asymmetrical environment confining the growth of the lobes. Inversely, this suggests young PS sources that are not frustrated may be more likely to show a symmetrical morphology like that of a CSO. MRC 0225–065 has a very symmetrical morphology according to our LBA images, suggesting it may not be interacting with its surrounding environment.

Linear size and turnover relation: We find MRC 0225–065 is entirely consistent with the linear size turnover relation, a natural product of the youth scenario. Although, it can be reproduced in certain frustration models.

Host galaxy: Using the MIR colours reported in by *WISE* and the optical spectrum from SDSS, we identify the MRC 0225–065 as having an obscured AGN with moderate star formation. Since the AGN does not dominate the entire MIR and optical emission, and there is still star formation present, it is possible the AGN has only recently been switched on and thus has not yet quenched all star formation in the galaxy, which is not surprising given the compact size of MRC 0225–065.

Magnetic field: Estimating the magnetic field using a purely SSA model and comparing it to the magnetic field calculated assuming equipartition are entirely consistent, suggesting the SSA model is a reasonable model for MRC 0225–065

Spectral ages: Using spectral modelling of the break frequency, we estimate the age of the radio emission (from the core and lobes) to be roughly 700 yr, consistent with estimates of the age of PS sources in the youth scenario.

Dynamical ages: Using the linear size from our LBA images and previous measurements of expansion velocity we estimate MRC 0225–065 has two major epochs of activity, one between 1 000 to 7 000 yr ago and another more recently from 100 to 900 yr ago. This is also consistent with previous estimates of the ages for young PS sources. Furthermore, due to the missing flux density at 8.3 GHz, this estimate should be considered an upper limit as the spectral indices for each component may be artificially steepened by the missing flux density.

We therefore conclude, MRC 0225–065 is likely a young AGN and with the peak occurring due to SSA.

Likewise, combining all information of PMN J0322–4820, we can also begin to create a unified picture that PMN J0322–4820 is a blazar. A summary of the evidence for this conclusion are:

Spectral variability: R21 identified PMN J0322–4820 as a variable source in and classified it as showing a changing spectral shape. The dramatic change in spectral shape in the megahertz regime on a timescale of ∼1 yr is inconsistent with evolutionary models for PS sources and predicted variability due to RISS. The changing spectral shape is most easily explained by the dynamical nature of blazars.

Radio morphology: The high resolution image of PMN J0322–4820 using the LBA found it was still compact on mas scales. This is also entirely consistent with a blazar morphology, which appears compact due to orientation effects.

Linear size and turnover relation: PMN J0322–4820 sits well below the linear size and turnover relation typically associated with PS sources. This could either be because it is a frustrated source and is thus more compact than expected for it's predicted age. However, more likely, is that the temporary peak detected with the MWA in 2014 was a result of the variability of a blazar with effects like Doppler boosting influencing measurements and thus the spectral peak is unrelated to the source age or absorption mechanisms.

WISE MIR Colours: PMN J0322–4820 has *WISE* colours typically associated with elliptical galaxies and/or LERGs/BL Lac blazars.

We therefore identify PMN J0322–4820 as a new blazar where the jets are oriented along the line-of-sight. However, PMN J0322–4820 was not in the ROMA-bzcat catalogue of γ-ray emitting blazars. This is potentially due to the steep spectrum at frequencies over 1 GHz where PMN J0322–4820 is too faint to be detected by traditional blazar searches. We suggest further observations using higher frequency observations in the X-ray or γ regimes to search for any high frequency counterpart (Massaro et al. 2009, 2015). We conclude PMN J0322–4820 should not be included in any future population studies of PS sources as it is a contaminating blazar and not a genuine PS source. Furthermore, this highlights the possibility of a population of blazars with steep spectra at high frequencies ($\nu \geq 1$ GHz) that are not detected in traditional blazar searches and thus may be contaminating populations of PS sources. Low-frequency spectral variability thus presents as a new method for identifying blazar candidates.

7. Conclusion

We have sought to compare detections of spectral variability for two PS sources with small scale (∼mas) morphology and structures. The images produced using observations with the LBA have identified one resolved and one unresolved PS source. We have also combined our observations with archival observations of the host galaxies of our sources to provide evidence for either the youth or frustration scenario.

We find PMN J0322–4820 is unresolved with the LBA at 2.4 GHz, and pace an upper limit of the source size to be 148 pc, using a photometric redshift of 0.16. In R21, PMN J0322–4820 was found to show a changing spectral shape and was presented as a blazar candidate. Comparing our compact morphology with the spectral variability of R21, we find PMN J0322–4820 is consistent with a blazar classification, and suggest high frequency (X-ray or Gamma) to confirm.

We resolve MRC 0225–065 into three components at both 2.4 and 8.3 GHz: a bright central region containing ∼50% of the total flux density, and two fainter regions roughly equal distance from the central region. In R21 and R22, MRC 0225–065 was found to show low levels of variability with a constant spectral shape, and presented as showing variability due to ISS from a compact morphology with resolved structure on mas scales. We find the projected linear size to be 430 pc, using a spectroscopic redshift of 0.445. Using spectral modelling, we calculate

the magnetic field assuming a purely SSA model, and find it is in agreement with the magnetic field calculated assuming equipartition. We therefore conclude MRC 0225–065 is a young CSO, with a PS classification due to SSA. We found the core to have a spectral age of $\tau_{spec} = 700 \pm 100$ yr, which is consistent with previous age estimates of young CSO sources of 10^1–10^5 yr (Orienti et al. 2010; Orienti & Dallacasa 2020). Furthermore, we use the spectral age of the core and the upper limit of core size to calculate and expected expansion velocity (assuming the simple relation speed = distance/time), and place an upper limit on the expansion velocity of the lobes to be $v = 0.13c$, well within previous measurements of expansion velocities for PS sources of $0.1c \lesssim v \lesssim 0.7c$ (Orienti & Dallacasa 2020). Lastly, we use this to estimate the dynamical age of the outer lobes and estimate their age to be $\tau_{dyn} \approx 5\,000$ yr, again, well within previous estimates of ages for young PS sources.

Our findings highlight the advantage of spectral variability in identifying different milliarcsecond structures in PS sources traditionally acquired using VLBI. Furthermore, we have confirmed the use of identifying contaminating sources displaying only a temporary spectral peak and present spectral variability as a new method for identifying steep spectrum blazars. We also suggest future observations of MRC 0225–065 to search for direct observations of expansion to better constraining the expansion velocity and age. We recommend observations of MRC 0225–065 with the VLBA for improved sensitivity and more u,v-coverage on short baselines to recover more flux density from extended structures. Likewise, with improved accuracy of the position for MRC 2236-454, we suggest another VLBI observation.

Reference

Albareti, F. D., et al. 2017, ApJS, 233, 25

An, T., & Baan, W. A. 2012, ApJ, 760, 77

Astropy Collaboration, e t al. 2013, A&A, 558, A33

Bicknell, G. V., Mukherjee, D., Wagner, A. Y., Sutherland, R. S., & Nesvadba, N. P. H. 2018, MNRAS, 475, 3493

Bilicki, M., Jarrett, T. H., Peacock, J. A., Cluver, M. E., & Steward, L. 2014, ApJS, 210, 9

Briggs, D. S. 1995, PhD thesis, New Mexico Institute of Mining and Technology

Buchner, J. 2021, JOSS, 6, 3001

Callingham, J. R., et al. 2015, ApJ, 809, 168

Callingham, J. R., et al. 2017, ApJ, 836, 174

Chhetri, R., Morgan, J., Ekers, R. D., Macquart, J. P., Sadler, E. M., Giroletti, M., Callingham, J. R., & Tingay, S. J. 2018, MNRAS, 474, 4937

Condon, J. J., Cotton, W. D., Greisen, E. W., Yin, Q. F., Perley, R. A., Taylor, G. B., & Broderick, J. J. 1998, AJ, 115, 1693

D'Abrusco, R., et al. 2019, ApJS, 242, 4

Deller, A. T., et al. 2011, PASP, 123, 275

Fanti, R., Ficarra, A., Mantovani, F., Padrielli, L., &Weiler, K. 1979, A&AS, 36, 359

Gugliucci, N. E., Taylor, G. B., Peck, A. B., & Giroletti, M. 2005, ApJ, 622, 136

Hale, C. L., et al. 2021, PASA, 38, e058

Hardcastle, M. J., & Looney, L. W. 2008, MNRAS, 388, 176

Hernández-García, L., et al. 2019, MNRAS, 489, 4049

Hinshaw, G., et al. 2013, ApJS, 208, 19

Hunter, J. D. 2007, CSE, 9, 90

Hurley-Walker, N., et al. 2019, PASA, 36, e048

Intema, H. T. Jagannathan, P., Mooley, K. P. & Frail, D. A. 2017, A&A, 598, A78

Jarrett, T. H., et al. 2011, ApJ, 735, 112

Keim, M. A., Callingham, J. R., & Röttgering, H. J. A. 2019, A&A, 628, A56

Kellermann, K. I., & Pauliny-Toth, I. I. K. 1981, ARA&A, 19, 373

Kettenis, M., van Langevelde, H. J., Reynolds, C., & Cotton, B. 2006, in Astronomical Society of the Pacific Conference Series, Vol. 351, Astronomical Data Analysis Software and Systems XV, ed. C. Gabriel, C. Arviset, D. Ponz, & S. Enrique, 497

Large, M. I., Cram, L. E., & Burgess, A. M. 1991, The Obs, 111, 72

Large, M. I., Mills, B. Y., Little, A. G., Crawford, D. F., & Sutton, J. M. 1981, MNRAS, 194, 693

Lonsdale, C. J., et al. 2015, ApJ, 813, 45

Marr, J. M., Perry, T. M., Read, J., Taylor, G. B., & Morris, A. O. 2014, ApJ, 780, 178

Marscher, A. P. 1983, ApJ, 264, 296

Martí-Vidal, I., Roy, A., Conway, J., & Zensus, A. J. 2016, A&A, 587, A143

Massaro, E., Giommi, P., Leto, C., Marchegiani, P., Maselli, A., Perri, M., Piranomonte, S., & Sclavi, S. 2009, A&A, 495, 691

Massaro, E., Maselli, A., Leto, C., Marchegiani, P., Perri, M., Giommi, P., & Piranomonte, S. 2015, Ap&SS, 357, 75

Mauch, T., Murphy, T., Buttery, H. J., Curran, J., Hunstead, R. W., Piestrzynski, B., Robertson, J. G., & Sadler, E. M. 2003, MNRAS, 342, 1117

McConnell, D., et al. 2020, PASA, 37, e048

[f]http://ds9.si.edu/site/Home.html.

McMullin, J. P., Waters, B., Schiebel, D., Young, W., & Golap, K. 2007, in Astronomical Society of the Pacific Conference Series, Vol. 376, Astronomical Data Analysis Software and Systems XVI, ed. R. A. Shaw, F. Hill, & D. J. Bell, 127

Miley, G. 1980, ARA&A, 18, 165

Murphy, T., et al. 2010, MNRAS, 402, 2403

O'Dea, C. P. 1998, PASP, 110, 493

O'Dea, C. P., & Baum, S. A. 1997, AJ, 113, 148

O'Dea, C. P., Baum, S. A., & Stanghellini, C. 1991, ApJ, 380, 66

O'Dea, C. P., & Saikia, D. J. 2021, A&ARv, 29, 3

Orienti, M., & Dallacasa, D. 2008, A&A, 487, 885

Orienti, M., & Dallacasa, D. 2014, MNRAS, 438, 463

Orienti, M., & Dallacasa, D. 2020, MNRAS, 499, 1340

Orienti, M., Dallacasa, D., Tinti, S., & Stanghellini, C. 2006, A&A, 450, 959

Orienti, M., Murgia, M., & Dallacasa, D. 2010, MNRAS, 402, 1892

Owsianik, I., & Conway, J. E. 1998, A&A, 337, 69

Pacholczyk, A. G., & Roberts, J. 1971, PhT, 24, 57

Pandas Development Team T. 2020, pandas-dev/pandas: Pandas, doi: 10.5281/zenodo.3509134, https://doi.org/10.5281/zenodo.3509134

Pérez, F., & Granger, B. E. 2007, CSE, 9, 21

Phillips, R. B., & Mutel, R. L. 1982, A&A, 106, 21

Polatidis, A. G., & Conway, J. E. 2003, PASA, 20, 69

Price-Whelan, A. M., et al. 2018, AJ, 156, 123

Readhead, A. C. S., Taylor, G. B., Pearson, T. J., & Wilkinson, P. N. 1996, ApJ, 460, 634

Ross, K., et al. 2021, MNRAS, 501, 6139

Ross, K., Hurley-Walker, N., Seymour, N., Callingham, J. R., Galvin, T. J., & Johnston-Hollitt, M. 2022, MNRAS, 512, 5358

Taylor, M. B. 2005, TOPCAT & STIL: Starlink Table/VOTable Processing Software, ed. P. Shopbell, M. Britton, & R. Ebert, 29

Tingay, S. J., & de Kool, M. 2003, AJ, 126, 723

Tingay, S. J., et al. 2015, AJ, 149, 74

Tinti, S., & de Zotti, G. 2006, A&A, 445, 889

Tinti, S., Dallacasa, D., de Zotti, G., Celotti, A., & Stanghellini, C. 2005, A&A, 432, 31

Torniainen, I., Tornikoski, M., Teräsranta, H., Aller, M. F., & Aller, H. D. 2005, A&A, 435, 839

Turner, R. J., Shabala, S. S., & Krause, M. G. H. 2018, MNRAS, 474, 3361

Tzioumis, A. K., et al. 2010, AJ, 140, 1506

van Breugel, W., Miley, G., & Heckman, T. 1984, AJ, 89, 5

van derWalt, S., Colbert, S. C., & Varoquaux, G. 2011, CSE, 13, 22

Virtanen, P., et al. 2020, NatM, 17, 261

Wells, D. C. 1985, Nrao'S Astronomical Image Processing System (AIPS) (Boston, MA: Springer US), 195, doi: 10.1007/978-1-4615-9433-8_18, https://doi.org/10.1007/978-1-4615-9433-8_18

WES McKinney 2010, in Proceedings of the 9th Python in Science Conference, ed. S. van der Walt, & J. Millman, 56, doi: 10.25080/Majora-92bf1922-00a

Wilkinson, P. N., Booth, R. S., Cornwell, T. J., & Clark, R. R. 1984, Natur, 308, 619

Wright, E. L. 2006, PASP, 118, 1711

Wright, E. L., et al. 2010, AJ, 140, 1868

Yang, X.-H., Chen, P.-S., & Huang, Y. 2015, MNRAS, 449, 3191